Phonon scattering rates and atomic ordering in $Ag_{1-x}Sb_{1+x}Te_{2+x}(x=0,0.1,0.2)$ investigated with inelastic neutron scattering and synchrotron diffraction

J. Ma, O. Delaire, E. D. Specht, A. F. May, O. Gourdon, J. D. Budai, M. A. McGuire, T. Hong, D. L. Abernathy, G. Ehlers, and E. Karapetrova

Phys. Rev. B **90**, 134303 — Published 7 October 2014

DOI: 10.1103/PhysRevB.90.134303

Phonon Scattering Rates and Atomic Ordering in $Ag_{1-x}Sb_{1+x}Te_{2+x}$ (x = 0, 0.1, 0.2) Investigated with Inelastic Neutron Scattering and Synchrotron Diffraction.

J. Ma,[1] O. Delaire,[2,*] E. D. Specht,[2] A. F. May,[2] O. Gourdon,[3] J. D. Budai,[2]
M. A. McGuire,[2] T. Hong,[1] D. L. Abernathy,[1] G. Ehlers,[1] and E. Karapetrova[4]

[1] *Quantum Condensed Matter Division, Oak Ridge National Laboratory, Oak Ridge, Tennessee 37831, USA*
[2] *Materials Science and Technology Division, Oak Ridge National Laboratory, Oak Ridge, Tennessee 37831, USA*
[3] *Los Alamos Neutron Science Center, Los Alamos National Laboratory, Los Alamos, NM 87545, USA*
[4] *Advanced Photon Source, Argonne National Laboratory, Argonne, IL 60439, USA*

(Dated: August 11, 2014)

The phonon dispersions and scattering rates of the thermoelectric material $Ag_{1-x}Sb_{1+x}Te_{2+x}$ (x = 0, 0.1, 0.2) were measured with inelastic neutron scattering, as function of both temperature T and off-stoichiometry x. In addition, detailed measurements of diffuse scattering were performed with both neutron and synchrotron x-ray diffraction. The results show that phonon scattering rates are large and weakly dependent on T or x, and the lattice thermal conductivity calculated from these scattering rates and group velocities is in good agreement with bulk transport measurements. We also find that the scattering rates and their temperature dependence cannot be accounted for with common models of phonon scattering by anharmonicity or point defects. The diffuse scattering measurements show a pervasive, complex signal, with several distinct components. In particular, broad superstructure reflections indicate a short-range ordering of the Ag and Sb cations on their sublattice. Single-crystal Bragg peak intensities also reveal large static atomic displacements, compatible with results from Rietveld refinement of neutron powder diffraction data. Our results indicate that a complex nanostructure, arising from multiple variants of nanoscale anisotropic superstructures of cations, and large atomic displacements, is likely responsible for the strong phonon scattering.

PACS numbers: 63.20.Mt, 78.70.Nx, 61.46.+w, 05.60.-k

I. INTRODUCTION

Thermoelectric materials are currently attracting significant interest as they can convert heat into electricity, and are thus relevant to a variety of energy technologies[1–3]. The performance of the materials used in the thermoelectric conversion process is quantified by the material figure-of-merit, $ZT = \alpha^2\sigma T/\kappa_{\rm tot}$, where α is the Seebeck coefficient, σ is the electrical conductivity, T is the absolute temperature, and $\kappa_{\rm tot}$ is the total thermal conductivity. In the case of non-magnetic materials, $\kappa_{\rm tot}$ is the sum of contributions from transport of electrical carriers, $\kappa_{\rm el}$, and from phonons propagating through the crystalline lattice, $\kappa_{\rm lat}$. We note that, while this separation of electronic and lattice degrees-of-freedom is justified in $AgSbTe_2$, it can fail in the case of strong electron-phonon coupling[4,5]. As $\kappa_{\rm el}$ is closely coupled to the electrical transport, which must be preserved, a widespread approach to optimizing ZT consists in suppressing $\kappa_{\rm lat}$.

The rocksalt chalcogenides are of wide interest in thermoelectric applications, in part because of their low thermal conductivities. For example, in PbTe $\kappa_{\rm lat} \simeq 2.2\,{\rm Wm^{-1}K^{-1}}$ at 300 K, further decreasing at higher temperatures owing to anharmonicity-dominated phonon scattering[6–9]. The compound $AgSbTe_2$ exhibits an even lower thermal conductivity, $\kappa_{\rm lat} \simeq 0.7\,{\rm Wm^{-1}K^{-1}}$ at 300 K, also showing a glass-like temperature-independent behavior[10–14]. In pure form, this compound exhibits a relatively high $ZT \approx 1.2$ at 720 K[3,15]. Furthermore, it is also used as a component in several other highly-efficient thermoelectric alloys, such as $(AgSbTe_2)_{1-x}(PbTe)_x$ and $(AgSbTe_2)_{1-x}(GeTe)_x$[3,16].

Previous studies have shown that the lattice contribution ($\kappa_{\rm lat}$) dominates $\kappa_{\rm tot}$ up to 300 K, while the electronic contribution is significantly smaller but increases with T (Ref. 10). Several mechanisms have been suggested to explain the very low, glass-like κ_{lat}, such as strong anharmonicity[12,17], force-constants differences around Ag and Sb atoms[18], and nano-precipitates[13,14,19–22]. However, the lack of direct microscopic measurements of the phonon scattering rates and mean-free-paths has hampered a detailed understanding.

The structure of $AgSbTe_2$ is derived from a rock-salt arrangement (δ–phase), with Ag^+ and Sb^{3+} sharing the cation sublattice. However, further complexity arises as the δ-phase is observed slightly off stoichiometry in the pseudo-binary Ag_2Te-Sb_2Te_3 phase diagram[19,23,24]. In addition, it has remained a long-standing question whether the cations are ordered or disordered on their sublattice[12,25–28]. While single-crystal x-ray diffraction and first-principles simulations identified ordered structures (such as $L1_1$ or $D4$ cation arrangements), the powder diffraction studies generally report a disordered-rocksalt arrangement[12–14,17].

Inelastic neutron scattering (INS) has been recognized as a powerful technique to study the microscopic origins of lattice thermal conductivity, as it directly measures the dynamical structure factor, $S(\mathbf{Q}, E)$, from which the phonon group velocities $v_j(\mathbf{q})$ and phonon lifetimes $\tau_j(\mathbf{q})$ can be extracted[29,31,32]. As such, INS offers a unique opportunity to rationalize the bulk lattice thermal conduc-

tivity from microscopic quantities, and provides crucial insights into the phonon scattering processes[5,29–32].

We have previously shown that the transverse acoustic modes provide the dominant contribution to the lattice thermal conductivity and that a complex nanostructure spontaneously present in the material is likely responsible for the low, glass-like thermal conductivity[32,33]. In the present paper, we report further measurements on the temperature and composition dependence of the phonon dispersions, phonon lifetimes, and phonon density of states. In addition, we also report extensive synchrotron x-ray scattering measurements on single-crystals, which provide detailed information about the complex diffuse scattering associated with short-range atomic ordering and strains. This more detailed analysis confirms that phonon-phonon umklapp and phonon-point defect scattering are not sufficient to account for the observed very low, glass-like κ. We conclude that strong phonon scattering by the nanostructure dominates and provides a temperature-independent disruption of phonon propagation from 10 to 300 K.

II. SAMPLE PREPARATION AND MEASUREMENTS

A. Synthesis and Characterization

Based on the phase diagram of Ag_2Te-Sb_2Te_3 (Refs. 19,23,24), a series of compounds $Ag_{1-x}Sb_{1+x}Te_{2+x}$ (x = 0, 0.1, and 0.2) were synthesized. Powder samples were prepared by direct fusion in sealed, evacuated, carbon-coated silica tubes. Single crystals were synthesized by a modified Bridgmann technique in silica ampoules with a tapered end. The compositions measured with electron-probe micro-analysis (EPMA) in the δ–phase were $Ag_{22.2}Sb_{26.8}Te_{51}$, $Ag_{21.5}Sb_{27.2}Te_{51.2}$, and $Ag_{18.5}Sb_{29.3}Te_{52.2}$ for nominal $x = 0, 0.1, 0.2$, respectively. From our transport measurements[32], we estimated a lattice-dominated thermal conductivity, $\kappa_{\rm lat} \simeq 0.65\,{\rm W}m^{-1}{\rm K}^{-1}$ at 200 K, and weakly dependent on T, which is in good agreement with prior reports in the literature[10–12,14].

B. Neutron powder diffraction

Neutron powder diffraction (NPD) measurements were performed with the POWGEN diffractometer[34] at the Spallation Neutron Source (SNS), Oak Ridge National Laboratory (ORNL). Ingots ($m \simeq 5\,g$) were ground into fine powders and loaded into vanadium containers. A close-cycled refrigerator (CCR) was used for low-temperature measurements, with the samples sealed in a partial atmosphere of helium. The measurements covered d-spacings from ∼0.4 to 2.5 Å. A vanadium standard was also measured to correct variations in efficiency of the detectors[34]. Additional high-T measurements were conducted in a radiative furnace, under vacuum.

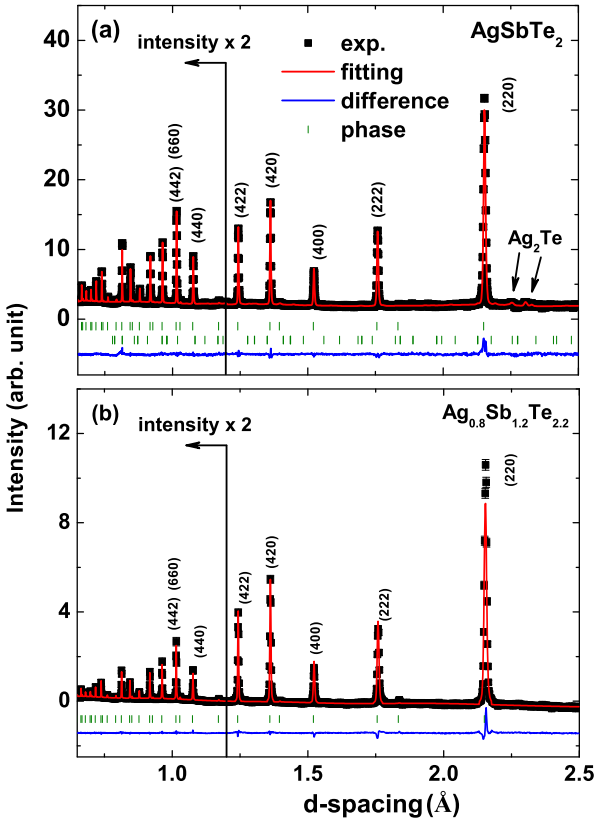

FIG. 1: Neutron diffraction patterns (black dots) and Rietveld refinements (red line) for $AgSbTe_2$(a) and $Ag_{0.8}Sb_{1.2}Te_{2.2}$ (b) at 300 K. Blues curves at the bottom of each panel are difference curves. The green tick marks in (b) are the reflection positions for the δ-phase of $AgSbTe_2$, while the green upper and lower tick marks in (a) are the reflection positions for the δ-phase of $AgSbTe_2$ and monoclinic phase of Ag_2Te, respectively. Intensities for $d < 1.2$ Å are scaled by a factor of 2 for improved readability.

Figure 1 shows NPD data at 300 K and Rietveld refinements obtained using the GSAS software package[35]. Previous experimental studies reported several possible ordered crystal structures, including cubic ($Pm\bar{3}m$), tegragonal ($P4/mmm$), and trigonal ($R\bar{3}m$) structures[27]. The refinement of the NPD data with these alternate space groups yields little improvement in the quality of the fits, in part because the neutron scattering lengths of Ag and Sb nuclei are very close ($b_{\rm Ag} = 5.92$ fm, $b_{\rm Sb} = 5.57$ fm, $b_{\rm Te} = 5.80$ fm). Because the atomic numbers are close for the three constituents, little contrast can also be expected in conventional powder x-ray diffraction. However, we show later that single-crystal neutron diffraction data reveals cation ordering, resulting in weak superlattice peaks. In the sample with $x = 0$, a secondary phase of monoclinic structure $P1\ 21/c\ 1$ was clearly observed, consistent with Ag_2Te, see Fig. 1(a). The amount

of Ag_2Te was estimated to be $\sim 6\%$ in this sample. The sample with $x = 0.2$ ($Ag_{0.8}Sb_{1.2}Te_{2.2}$) did not contain any observable amount of Ag_2Te phase (which was also confirmed by the absence in this sample of any latent heat signature for the monoclinic-cubic transformation of Ag_2Te at 418 K, often used to test for the presence of this secondary phase[14]).

C. Inelastic neutron scattering

INS measurements were performed on both powder and single-crystal samples with the ARCS time-of-flight chopper spectrometer at SNS, ORNL[36]. For higher resolution at low energy, the single-crystal samples were also measured with the cold neutron time-of-flight and triple-axis spectrometers, CNCS at SNS and CTAX at HFIR, ORNL[37].

For powder measurements, the samples were encased in a thin-walled aluminum cylinder of 12 mm diameter. The measurements were performed in a closed-cycle refrigerator for $10 \leqslant T \leqslant 300$ K. Measurements at high temperature were performed in a radiative furnace. All INS measurements were performed in vacuum. No oxidation or decomposition could be seen on the samples during the measurements. The incident neutron energy E_i was 25 meV, and the energy resolution was about 1.25 meV FWHM at the elastic line. The empty sample container was measured in identical conditions at all temperatures to allow for proper background subtraction. In this study, the wavevector transfer was integrated over the range $2.5 \leqslant Q \leqslant 4.2$Å^{-1}, corresponding to an averaging over phonon dispersions in about 10 Brillouin zones.

The contribution of single-phonon creation processes to the scattering function of a monatomic cubic material is given by[38],

$$S(Q,E) = \frac{\hbar^2 Q^2}{4M}\frac{g(E)}{E}\langle n(E)+1\rangle e^{-2W}\,, \qquad (1)$$

where $\hbar Q$ and E are the momentum and energy transfer to the sample, M, e^{-2W}, and $n(E)$ are the mass, Debye-Waller factor, and the Bose factor, and $g(E)$ is the phonon DOS. For non-monatomic structures, the measurement provides a neutron-weighted phonon DOS, $g_{\rm NW}(E)$, with each element contributing a partial phonon DOS weighted by the ratio of its neutron cross-section, σ, and mass, M (Ref. 39). However, for Ag, Sb, and Te, these ratios are close: σ/M = 4.63 × 10^{-2}, 3.20 × 10^{-2}, and 3.39 × 10^{-2} b/amu, respectively, thus $g_{\rm NW}(E) \simeq g(E)$ in the present case. In order to avoid the signal from the elastic peak, the data for $E \leqslant 2$ meV were cut and extrapolated with a Debye model. An iterative procedure was used to correct for the effect of multiphonon scattering.

Single-crystal INS measurements were conducted with the samples mounted in a CCR, and aligned with (H,H,L) as the primary scattering plane. Data were collected at

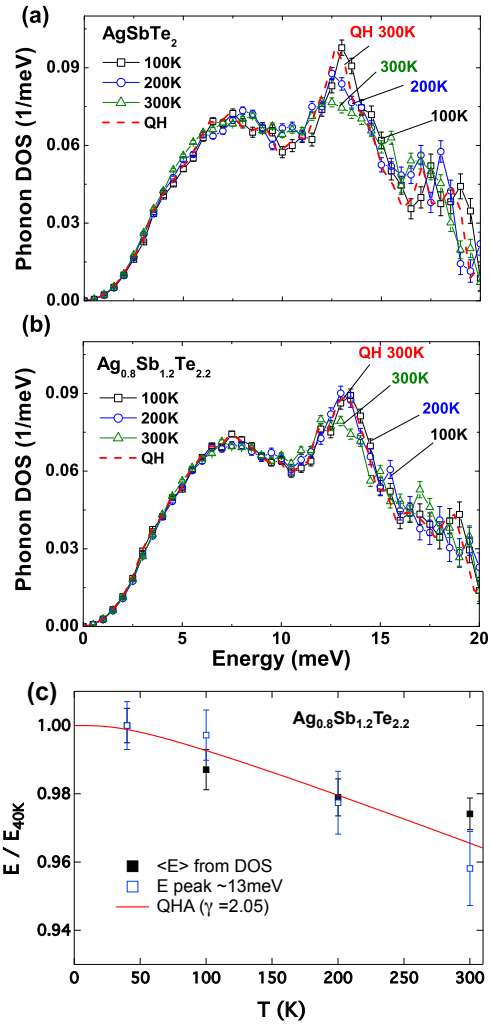

FIG. 2: Phonon DOSs measured at 100(black square line), 200(blue circle line), and 300 K(green triangle line) for $AgSbTe_2$(a) and $Ag_{0.8}Sb_{1.2}Te_{2.2}$(b). Dashed red lines (QH) is the quasiharmonic prediction for the phonon DOS at 300 K, given the measured DOS at 100 K (see text). Panel (c) shows a comparison of the temperature dependence of $\langle E\rangle$ and the energy of the peak around 13 meV in $Ag_{0.8}Sb_{1.2}Te_{2.2}$, compared with the QH model for $\gamma = 2.05$, and thermal expansion from Ref. 32.

T = 10, 100, 200, and 300 K on ARCS, T = 10, 100, and 300 K on CNCS, and T = 300 K on CTAX. An additional measurement on CNCS (300 K), not previously reported in Ref.[32], was performed with a $Ag_{0.8}Sb_{1.2}Te_{2.2}$ crystal mounted in the (H,K,0) scattering plane, to measure phonons with $q \parallel [1\bar{1}0]$, polarized along [110]. Measurements were performed with incident energies E_i = 25 meV on ARCS and 10.5 meV on CNCS, and with constant final energy E_f = 4 meV on CTAX. The corresponding energy resolutions (FWHM) at zero energy transfer for ARCS[36], CNCS[37] and CTAX were 1.25, 0.45, and 0.20 meV, respectively.

D. Synchrotron x-ray diffuse scattering

X-ray diffuse scattering measurements were made on single-crystals of $Ag_{0.8}Sb_{1.2}Te_{2.2}$ at the X-ray Operations and Research beamline 33-BM-C at the Advanced Photon Source (APS), Argonne National Laboratory[41]. An x-ray energy of 21.5 keV was selected based on considerations of sample transmission and detector efficiency, and were selected from bending-magnet radiation using a Si(111) double-crystal monochromator. The second crystal of the monochromator was dynamically bent to focus the beam horizontally to 1 mm FWHM. A Pd-coated mirror was dynamically bent to focus the beam vertically to 0.5 mm FWHM and to suppress higher-order reflections from the monochromator. Incident x-ray flux, typically 4.5×10^{11} photons/s, was measured using an air-filled ionization counter.

Measurements were performed on crystals of $Ag_{0.8}Sb_{1.2}Te_{2.2}$ with flat polished (111) and (001) faces. The mosaic of the polished surface was about 0.12° full-width-half-maximum. A closed-cycle helium refrigerator was used to cool the crystals to $T \sim 30$ K. The sample was attached with Ag-loaded conducting epoxy to the refrigerator Cu mount, held under vacuum. A Be hemisphere, 75 mm in diameter and 0.40 mm thick, served as an x-ray window. The CCR was mounted on a four-circle diffractometer with the polished face in reflection geometry. A circular x-ray aperture, 5 mm in diameter, was placed on the 2θ arm immediately downstream of the Be hemisphere, blocking scattering from air and from the hemisphere.

Scattered x-rays were measured using a Pilatus 100K detector, a 487×195 array of $172 \times 172\,\mathrm{mm}^2$ Si diodes, operating in single-photon counting mode. The detector was placed 530 mm from the sample on the 2θ arm. Calibrated Ti foils were used to attenuate the diffracted beam when the detector would otherwise saturate (i.e. close to Bragg reflections). Diffuse scattering volumes were measured by scanning θ through (typically) 14 degrees in 48 steps, collecting counts for 3 sec at each step. Larger reciprocal space volumes were measured by repeating these θ scans over a grid of 2θ and χ values.

III. RESULTS AND DISCUSSION

A. Phonon density of states

The temperature dependence of the neutron-weighted phonon DOS (measured with ARCS) of $AgSbTe_2$ and $Ag_{0.8}Sb_{1.2}Te_{2.2}$ is shown in Fig. 2. Within experimental uncertainties, the DOS is nearly identical for both compositions, indicating that the small Ag_2Te impurity phase has a very limited effect on the phonon spectra of the δ–phase, and that the phonon spectrum of Ag_2Te is also similar to that of the δ-phase. The DOS exhibits three broad peaks centered around 7, 13, and 17 meV. The instrument energy resolution was 1.25 meV FWHM at zero energy transfer, decreasing to 0.70 meV at 15 meV energy transfer. The general shape of the spectrum, in particular the presence of three main peaks, is in fair agreement with our previous first-principles calculation[32], although the measured DOS is somewhat broader, partly because the phonon linewidths were not included in the calculation. In comparison, computed phonon energies in Ref. 25 are about 15% lower than in our measurement.

The measured temperature dependence of the DOS between 100 and 300 K was compared with a quasiharmonic (QH) model of the phonon softening. In the QH approximation, the phonon frequencies and interatomic force-constants are assumed to depend on temperature only via the volume effect of thermal expansion. The dependence of the average phonon energy on volume is quantified by the average Grüneisen parameter, $\bar{\gamma}_G$,

$$\bar{\gamma}_G = -\partial \ln\langle E\rangle / \partial \ln V\,, \tag{2}$$

which can be expressed in terms of standard thermodynamic quantities,

$$\bar{\gamma}_G = \frac{\alpha V_m B_T}{C_V} = \frac{\alpha V_m B_S}{C_P}\,, \tag{3}$$

where α is the linear coefficient of thermal expansion, V_m is the molar volume, B_T (B_S) is the isothermal (isentropic) bulk modulus, and C_V (C_P) is the heat capacity at constant volume (constant pressure)[42]. Using the thermodynamic average Grüneisen parameter reported by Morelli *et al.*[12], $\bar{\gamma}_G \simeq 2.05$ for $AgSbTe_2$, and the thermal expansion reported in Ref. 32, we obtained the QH prediction for the phonon DOS at 300 K, based on the measured DOS at 100 K, see Fig. 2 (red dashed line). The agreement between this QH DOS and the measured DOS at 300 K is rather good, except for some broadening of the optical modes at 13 meV. Also, in Fig. 2-c, we show the temperature dependence for the average phonon energy and the peak around 13 meV, compared with the same QH model. Although uncertainties are significant, the agreement is good.

B. Phonon dispersions

The wavevector-dependent phonon dispersions and line-widths were obtained from measurements of large single-crystals of $Ag_{0.8}Sb_{1.2}Te_{2.2}$ and $Ag_{0.9}Sb_{1.1}Te_{2.1}$. In both compositions, the phonon modes are very broad. Figure 3(a) displays a map of the dynamical susceptibility $\chi''(\mathbf{Q}, E)$ of $Ag_{0.8}Sb_{1.2}Te_{2.2}$, showing intensity from the TA branch along the [001] direction, measured with ARCS in the Brillouin zone (440). In these measurements, the neutron wave vector transfer is $\mathbf{Q} = \mathbf{q} + \tau$, with τ the reciprocal lattice vector nearest to $\mathbf{Q}$ (in this figure, $\tau = (440)$). Throughout the discussion, we use reciprocal space coordinates (h, k, l) corresponding to on an average rock-salt lattice. We note that the Bragg peaks with all-even (h,k,l) are much stronger than other reflections, owing to the closely matched neutron scattering

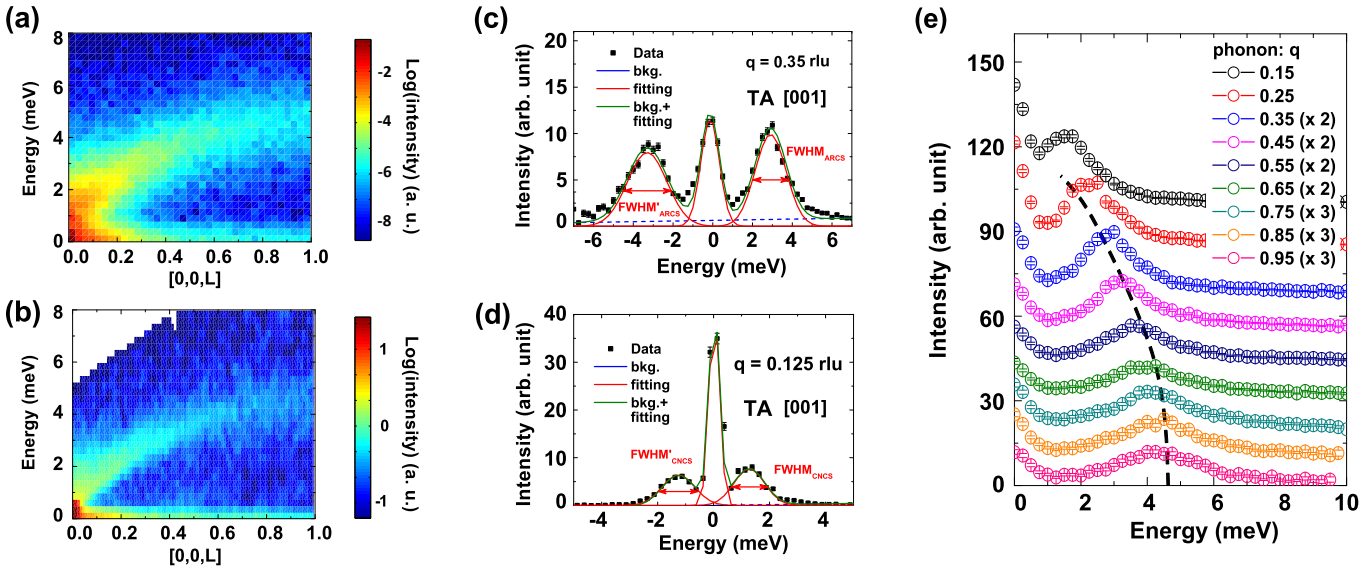

FIG. 3: (a, b) Neutron scattering intensity $\chi''(\mathbf{Q}, E) = (1\text{-}e^{2E/k_BT})S(\mathbf{Q}, E)$ showing TA dispersions along [001] at 300 K, measured with ARCS($E_i = 25$ meV, zone (440)) and CNCS($E_i = 10.5$ meV, zone (220)), respectively. (c, d) Fits of spectra for $Ag_{0.8}Sb_{1.2}Te_{2.2}$ measured with ARCS and CNCS for different wave-vectors q. The background is fit with a linear function, while the elastic scattering and the phonon peaks are fit with Gaussians. (e) Series of spectra from ARCS for q along [001]. The dashed line is a guide for the eye, indicating the center of the TA phonon peaks.

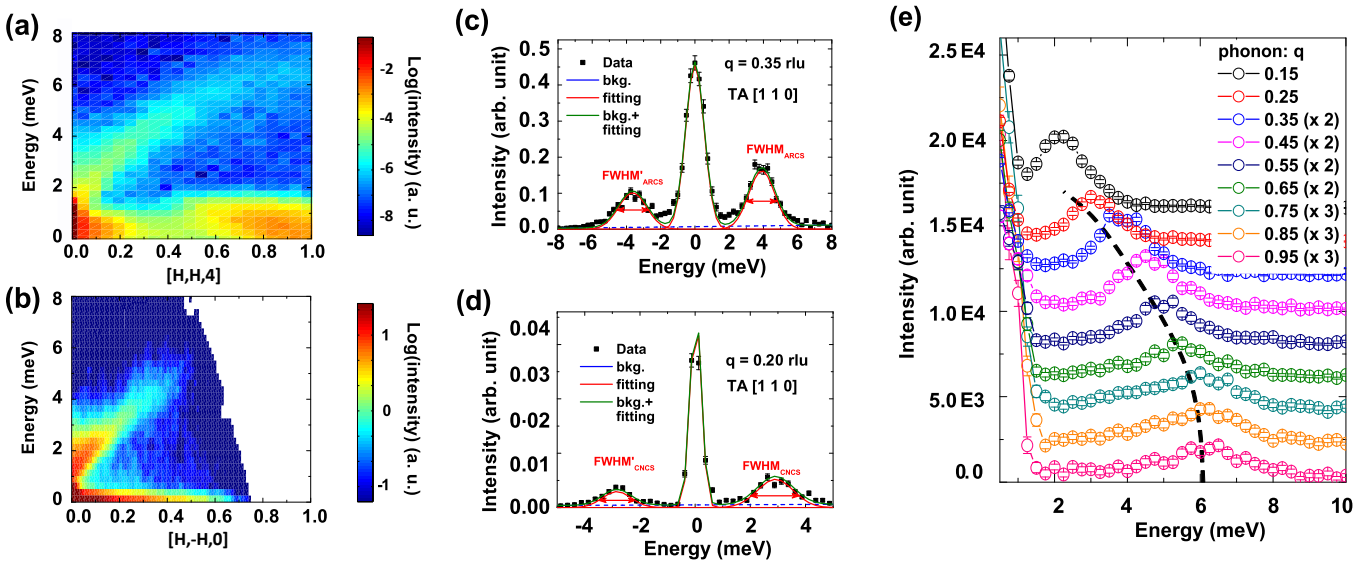

FIG. 4: (a, b) Neutron scattering intensity $\chi''(\mathbf{Q}, E) = (1\text{-}e^{2E/k_BT})S(\mathbf{Q}, E)$ showing TA dispersions along [110] at 300 K, measured with ARCS ($E_i = 25$ meV, zone (004)) and CNCS ($E_i = 10.5$ meV, zone (220)), respectively. We note that in panel (a), the intensity at low energy ($E < 2$ meV) for $H > 0.6$ rlu corresponds to background from an Al diffraction ring, as may be seen in Fig. 10-a. Panel (b) shows data for phonons with $q \parallel [1\bar{1}0]$, polarized along [110], from a measurement with the crystal mounted in (H,K,0) plane (CNCS, 300 K). (c, d) Fits of spectra for $Ag_{0.8}Sb_{1.2}Te_{2.2}$ with ARCS and CNCS for different q. The background is fit with a linear function, while the elastic scattering and the phonon peaks are fit with Gaussian functions. (e) Series of spectra from ARCS for q along [110]. The dashed line is a guide for the eye, indicating the center of the TA phonon peaks.

lengths of cations and anions. Thus, the dispersions of acoustic phonons were extracted mainly from the even Brillouin zones.

Fig. 3 shows INS intensities for TA phonons with wave vectors q along [001]. An example constant-Q spectrum from ARCS data for $q = 0.35$ (measured with $E_i = 25\,\mathrm{meV}$, $T = 300\,\mathrm{K}$) is presented in Fig. 3(c). It was obtained with an integration range of $\Delta Q_{[001]} = \pm 0.05\,\mathrm{rlu}$ (reciprocal lattice units) at each step ($\Delta Q_{[110]} = \pm 0.15\,\mathrm{rlu}$, and $\Delta Q_{[1\bar{1}0]} = \pm 0.15\,\mathrm{rlu}$). The CNCS data allow the extraction of the phonon line-width for smaller q values, owing to the better instrumental resolution. Panel 3(d) shows a spectrum from CNCS data ($E_i = 10.5$ meV) for a phonon wave vector $q = 0.125\,\mathrm{rlu}$ (integration range $\Delta Q_{[001]} = \pm 0.025\,\mathrm{rlu}$, $\Delta Q_{[110]} = \pm 0.1\,\mathrm{rlu}$, $\Delta Q_{[1\bar{1}0]} = \pm 0.1\,\mathrm{rlu}$). In both ARCS and CNCS measurements (Fig. 3(a,b)), the TA phonon branch is clearly observed, corresponding to a sharp peak at low-q, gradually broadening with increasing q. In panel 3(e), one may clearly see that the phonon peaks become broader at higher q values, besides dispersing to higher energies. One should note that the instrumental resolution (for both ARCS and CNCS) becomes sharper at larger energy[36,37], and thus this cannot account for the phonon peak broadening. Rather, this broadening results from the change in intrinsic phonon line-width. The panels in Fig. 4 show results for phonons along [110], with the same integration ranges as Fig. 3.

The data shown in Figs. 3 and 4, as well as additional data at different temperatures, were analyzed to extract the dispersion curves and line-widths. The elastic scattering and phonon peaks could be fit satisfactorily with Gaussians (see panels 3(c,d) and 4(c,d)). The phonon peaks at positive or negative energy transfers have different widths, owing to the energy-dependent instrumental resolution, which improves for larger positive energy transfer ($E > 0$ corresponds to phonon creation, and $E < 0$ to phonon annihilation), and also because of the asymmetric energy resolution in the case of ARCS data (which causes a 'bleeding' of the elastic line into the range $E < 0$)[36]. For both CNCS and ARCS measurements, only the part of the data with $E > 0$ was retained in subsequent analysis. The respective energy-dependent resolutions of the different instruments used were taken into account to extract the intrinsic phonon line widths (assuming gaussian resolutions with energy-dependent width[36,37]). The Q-resolution was obtained from the width of the Bragg peaks and the size of the Q-integration volume. The effect of dispersion slopes on the effective energy resolution was also taken into account, using the measured dispersions and the Q-resolution. The uncertainties in the measured phonon energies and line-widths result from the statistical uncertainties in fitting the phonon peaks, and the propagated uncertainties from the dispersion slope.

Figure 5 displays the resulting phonon dispersions, $E(\mathbf{q})$, and line-widths, $2\Gamma(\mathbf{q})$, for TA branches along [001], [110] (TA branch polarized along [001]), and [111]

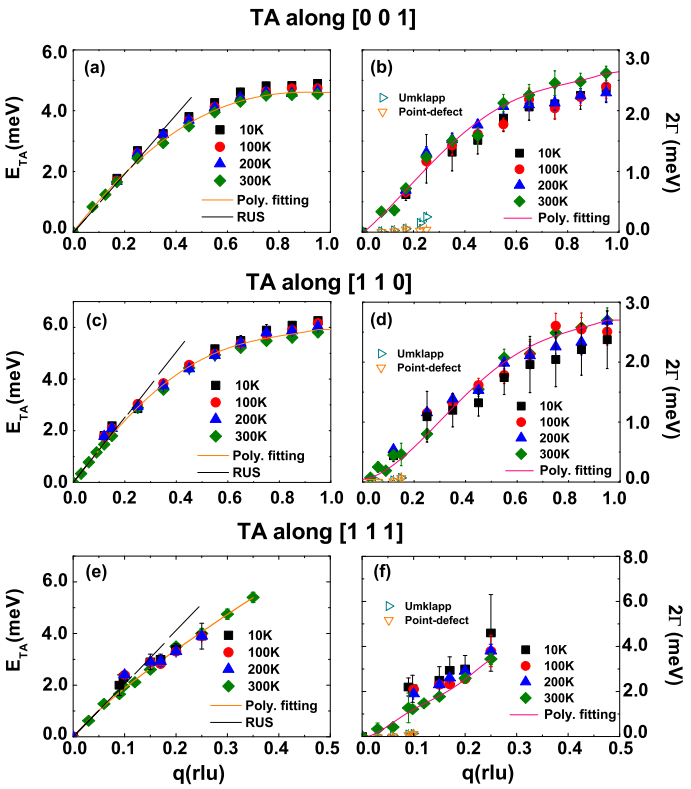

FIG. 5: Temperature dependence of the phonon dispersions and line-widths in $Ag_{0.8}Sb_{1.2}Te_{2.2}$, along the crystallographic directions [001] (a, b), [110] (c, d), and [111] (e,f), combining data obtained with CTAX (for $q \leqslant 0.15$), CNCS, and ARCS ($q \geqslant 0.25$) spectrometers. The dashed black lines indicate the limit of dispersion slopes for $q \to 0$, corresponding to elastic constants from resonant ultrasound measurements (RUS) at 300 K (Ref. 32). The thin orange and pink lines are polynomial fits to the phonon dispersion energies and line-widths, respectively, at 300 K.

(polarized along [1,1,-2]), as a function of temperature T =10, 100, 200, 300 K. One can observe a small decrease of phonon energies with increasing temperature, for both [001] and [110] directions (Figs. 5-a,c). Concurrently, the line-widths increase slightly with T, on average about 10% between 10 and 300 K, although the change is not much larger than the experimental uncertainties. This represents a small change in phonon scattering rates, and indicates that the predominant phonon scattering mechanism is largely independent of temperature.

Our measured phonon dispersions do not show any lattice instabilities at any wave vector, which would appear as a pronounced dip in the dispersion and increased line-width. We find a very good agreement between the long-wavelength limit of the dispersions from INS for $q \to 0$, and the linear limit $\omega \propto q$ from elastic constants measured with resonant ultrasound measurements (RUS)[32]. The TA dispersions start to deviate from this linear behavior around $q \gtrsim 0.2\,\mathrm{rlu}$, along both [001] and [110], and

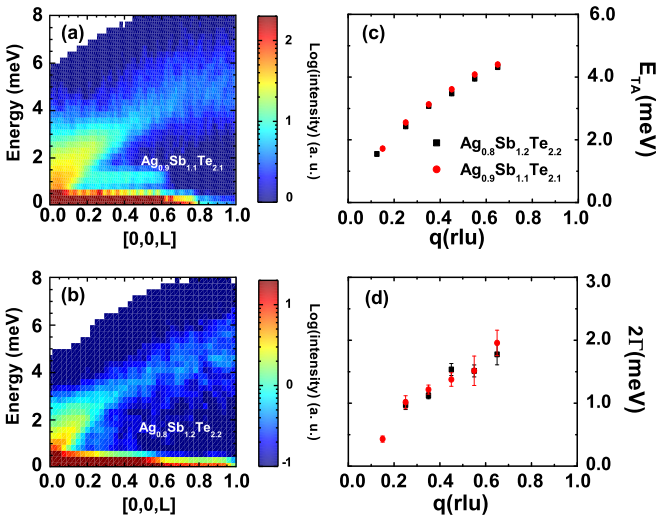

FIG. 6: (a,b) Scattering intensity maps for $Ag_{0.1}Sb_{1.1}Te_{2.1}$ and $Ag_{0.8}Sb_{1.2}Te_{2.2}$, respectively, measured with CNCS at 100 K. (c,d) Comparison of phonon dispersions and line-widths for TA phonons along $[0, 0, L]$ at 100 K, for these two compositions.

around $q \gtrsim 0.15$ rlu, along [111].

A comparison of TA dispersions and line-widths in the crystals with nominal compositions $Ag_{0.8}Sb_{1.2}Te_{2.2}$ and $Ag_{0.1}Sb_{1.1}Te_{2.1}$ is shown in Fig. 6, for the direction [001]. Panels (a,b) show the scattering intensity maps obtained with CNCS at 100 K, and panels (c,d) show the extracted phonon energies and line-widths. As can be seen, both the phonon dispersions and the line-widths are nearly identical for the two compositions. Since the vacancy concentration is expected to be different in the two crystals (from compositions measured with EPMA), these results suggest that scattering by vacancies is not the predominant source of phonon scattering. This conclusion is further corroborated by a calculation of the expected contribution of point-defect scattering (see below). It is possible that point-defect scattering affects optic modes more. Figure 7 shows that optic modes are completely damped, which was observed at all temperatures, and for both compositions. This behavior is strikingly different from the case of PbTe or SnTe, which both show well defined optic branches at 300 K (see Refs. 29,30).

Correlation plots between phonon relaxation times and frequency or wave-vector are presented in Fig. 8, comparing $AgSbTe_2$ with PbTe. The phonon linewidths for PbTe were obtained with CNCS (details of measurements are described in Ref. 29). As can be seen on this figure, the phonon lifetimes in PbTe are substantially larger than in $Ag_{0.8}Sb_{1.2}Te_{2.2}$ for all TA phonons at 300 K, in agreement with the κ_{lat} being three times larger in PbTe than in $Ag_{0.8}Sb_{1.2}Te_{2.2}$. Also, we note that the phonon lifetimes in $Ag_{0.8}Sb_{1.2}Te_{2.2}$ are shortest along the [111] direction, although the group velocities are largest in that direction, for both TA and LA branches.

C. Lattice thermal conductivity

As was discussed in previous section, comprehensive information about the phonon group velocities and scattering rates was gained from the INS measurements. This information can be utilized to build a microscopic understanding of the lattice thermal conductivity, which can be compared to bulk transport data. We only included acoustic modes in our analysis, as the optic phonons appeared fully damped (Fig. 7), and should thus have a minimal contribution to thermal conductivity. The contribution of the phonon mode of wavevector $\mathbf{q}$ and branch index j to the lattice thermal conductivity is given by[43]:

$$\kappa_{\mathrm{lat},j}(\mathbf{q}) = \frac{1}{3} C_{ph}(E_j(\mathbf{q})) v_j^2(\mathbf{q}) \tau_j(\mathbf{q}) \,, \qquad (4)$$

where $C_{ph}(E_j(\mathbf{q}))$ is the phonon specific heat, and $v_j(\mathbf{q})$ and $\tau_j(\mathbf{q})$ are the group velocity and the lifetime of the phonon mode ($\mathbf{q}$, j), respectively. In order to compute the total lattice thermal conductivity from INS data, we obtain the group velocities from the gradient of the measured phonon dispersions, $v_j(\mathbf{q}) = |\nabla_q \omega_j(\mathbf{q})|$, and the relaxation times τ are obtained from the line-widths, $2\Gamma_j(\mathbf{q}) = h\tau_j^{-1}(\mathbf{q})$. Both $\omega_j(\mathbf{q})$ and $2\Gamma_j(\mathbf{q})$ were interpolated with polynomials to perform the calculations, as illustrated in Fig. 5. In order to integrate the contributions of individual modes ($\mathbf{q}$, j) over the entire Brillouin zone, we perform a spherical integration over high-symmetry directions, $\hat{\eta}$, followed with a weighted-average for the multiplicity of each direction:

$$\kappa_{\mathrm{lat},\hat{\eta},j} = 4\pi \int_0^{q_{\mathrm{max},\hat{\eta}}} \kappa_{\mathrm{lat},j}(q\,\hat{\eta}) q^2 dq \,, \qquad (5)$$

where $q_{\mathrm{max},\hat{\eta}}$ is dependent on the geometry of the Brillouin zone and the crystallographic direction $\hat{\eta}$. The average over directions and branch index was then performed,

$$\kappa_{\mathrm{lat}} = \sum_{i,j} f_i \kappa_{\mathrm{lat},\hat{\eta}_i,j} \,, \qquad (6)$$

with f_i the multiplicities of different crystallographic directions $\hat{\eta}_i$ and j the branch index. From this analysis, we derive a lattice thermal conductivity $\kappa_{\mathrm{lat}} = 0.8 \pm 0.15\,\mathrm{W}m^{-1}\mathrm{K}^{-1}$ for $Ag_{0.8}Sb_{1.2}Te_{2.2}$ at 300 K. This result is in remarkable agreement with the estimated value from our transport measurements, as well as values reported in the literature ($\kappa_{\mathrm{lat}} \simeq 0.7\,\mathrm{W}m^{-1}\mathrm{K}^{-1}$)[10–14]. In addition, our results show that the transverse acoustic (TA) phonons contribute about 80% of κ_{tot}. The good

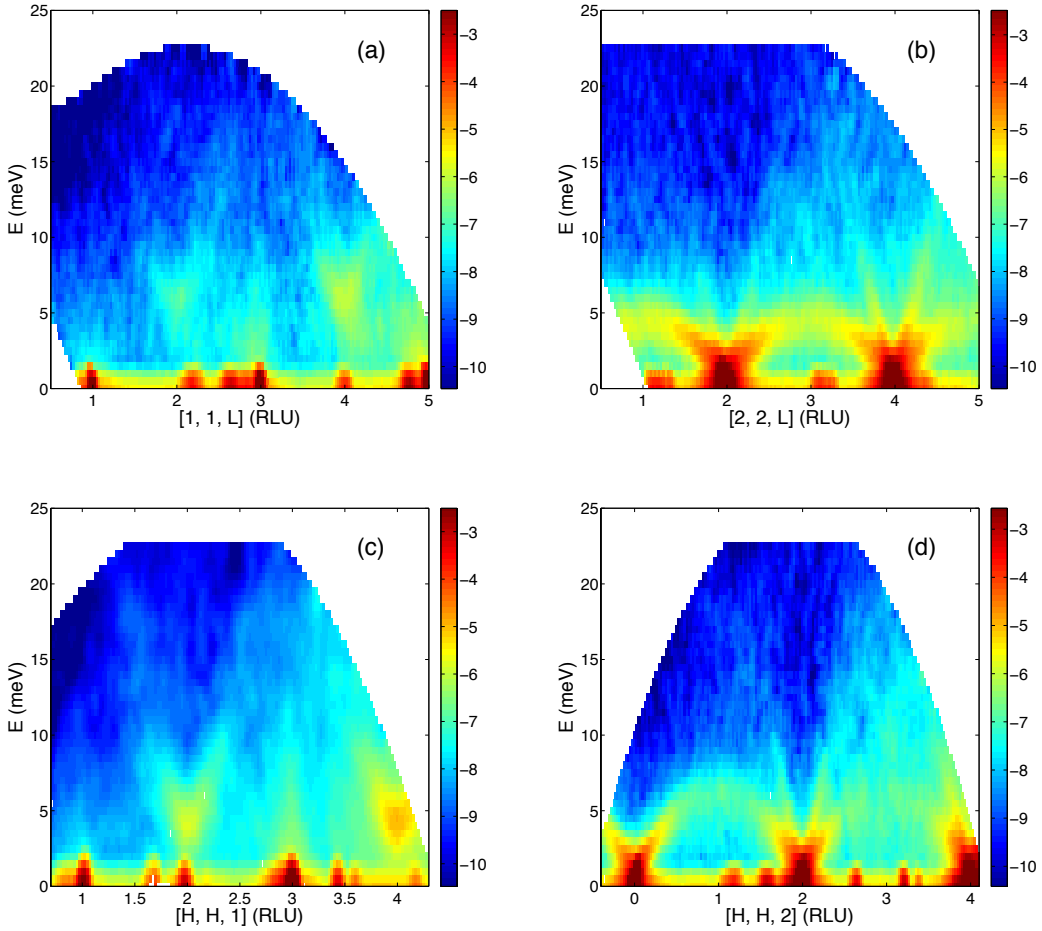

FIG. 7: Scattering intensity, $S(\mathbf{Q}, E)$, for $Ag_{0.8}Sb_{1.2}Te_{2.2}$ measured with ARCS at 300 K, with $E_i = 25$ meV. These views show the very broad nature of optical modes for $8 \leqslant E \leqslant 20$ meV. In (a,b), the integration ranges are $\Delta Q_{[110]} = \pm 0.1$ rlu, and $\Delta Q_{[1\bar{1}0]} = \pm 0.1$ rlu. In (b,c), they are $\Delta Q_{[001]} = \pm 0.1$ rlu, and $\Delta Q_{[1\bar{1}0]} = \pm 0.1$ rlu. Intensity scale is logarithmic.

agreement with transport measurement confirms that optic modes should have a negligible contribution. As noted earlier, we have found that the mean-free-paths are shortest along [111]. We discuss later how the cations tend to order in a superstructure, which can break the cubic symmetry, although because of the short-range nature of the correlations, the system remains cubic on average. Also, because the mean-free-paths are very short, the tensor for $\kappa_{\rm lat}$ is of rank-2, instead of the rank-4 elastic tensor, which governs ballistic transport. As a result, the rank-2 $\kappa_{\rm lat}$ tensor of the cubic system is isotropic, and this was confirmed in our measurements[32]. The phonon data for $Ag_{0.9}Sb_{1.1}Te_{2.1}$ were less complete and the full integration was not performed in this case. However, because of the strong similarity of dispersions and line-widths along [001] for the two compositions, as well as the similarity of their phonon DOS, it is expected that a very similar value for $\kappa_{\rm lat}$ would be obtained in $Ag_{0.9}Sb_{1.1}Te_{2.1}$.

D. Analysis of scattering rates

In the following, we compare our INS data with widely-used models of phonon-phonon scattering and phonon–point-defect scattering.

1. *Phonon-phonon umklapp scattering*

As originally shown by Peierls[44], phonon-phonon umklapp scattering is expected to exhibit a pronounced temperature dependence, on a scale comparable with the Debye temperature θ_D,

$$\tau_u^{-1} \propto T^n e^{\theta_D/(m\,T)}\,, \qquad (7)$$

where n and m are constants on the order of unity. From the phonon DOS of $Ag_{0.8}Sb_{1.2}Te_{2.2}$ at 300 K, we obtained $\theta_D = 155$ K (using the relation $\theta_D = 4/3\langle E\rangle$).

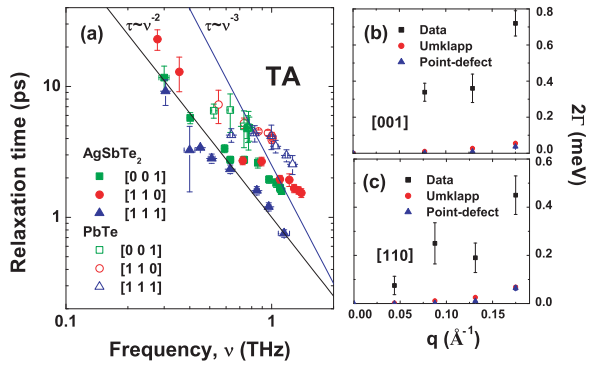

FIG. 8: (a) Frequency-dependent phonon relaxation times of $Ag_{0.8}Sb_{1.2}Te_{2.2}$ and PbTe at 300 K. The solid lines denote $\tau = 1 \times 10^{12}\ \nu^{-2}$, and $\tau = 2.5 \times 10^{24}\ \nu^{-3}$. (b) and (c) Comparisons of the measured line-widths and calculations of the contributions from the umklapp phonon-phonon and point-defect scatterings of TA phonon mode of $Ag_{0.8}Sb_{1.2}Te_{2.2}$ along [001] and [110] as a function of q at 300 K.

An estimate based on acoustic phonon branches alone would be lower, roughly $\theta_D \sim 100\,\mathrm{K}$. With either estimate, the magnitude of phonon-phonon umklapp scattering would be expected to vary significantly over the range of temperatures measured in the present study ($10 \leqslant T \leqslant 300\,\mathrm{K}$). Thus, the limited measured variation in phonon line-widths indicates that phonon-phonon umklapp scattering is not the dominant process below 300 K.

Based on the model of Leibfried and Schlomann, Slack *et al.*[45,46] proposed a more detailed expression, using the Grüneisen constant, the sound velocity, and the average atomic mass M, applicable for $0.05 \leqslant \frac{T}{\theta_D} \leqslant 2$:

$$\tau_u^{-1} \approx \frac{\hbar\gamma^2}{Mv^2\theta_D}\omega^2 T e^{-\frac{\theta_D}{3T}}\,, \qquad (8)$$

The phonon frequency ω and the group velocity v at each q were obtained from our INS measurements. We note that this model is limited to the Debye regime (low q), as it would diverge at larger q where the group velocity v becomes zero. Thus we limited the evaluation of the expression to $|q| < 0.2\,\mathrm{Å}^{-1}$, based on the dispersions in Fig. 5. The results for line-widths $2\Gamma_u = \tau_u^{-1}$ are plotted in Fig. 8(b, c). Although the contribution of umklapp scattering is increasing with $\mathbf{q}$, $2\tau_u^{-1}$ is much smaller than the measured line-widths, at most 15% of the observed value at 300K.

2. Phonon–point-defect scattering

The point-defect is another possible phonon scattering source due to the disorder of Ag/Sb in the cation sublattice, and the presence of cation vacancies or Te antisite defects. Based on Klemens' calculation on the relaxation rate for phonon–point-defect scattering where the linear dimensions of the defects are much smaller than the phonon wavelength, the corresponding phonon–point-defect scattering rate is taking into account both the mass and force-constant difference effect[47],

$$\tau_{pd}^{-1} = \frac{V}{4\pi v^3}\omega^4 \sum_i f_i\left[\frac{\bar{m}-m_i}{\bar{m}} + \frac{2(\bar{k}-k_i)}{2\bar{k}-k_i}\right]^2, \qquad (9)$$

where V is the volume per atom, m_i and k_i are the mass and force-constant of defect i, $\bar{m}$ and $\bar{k}$ are the average mass and force-constant of all atoms, and f_i is the fraction of defect i. Here again, the evaluation is limited to the linear part of the phonon dispersions $|q| < 0.2\,\mathrm{Å}^{-1}$.

For $AgSbTe_2$, the on-site diagonal force constants of Ag, Sb, and Te are quite different: 2.16, 4.72, and 4.08 (units in $\times\ 10^4$ *dyn/cm*), respectively[18]. If 5% vacancies are considered, the estimate of line-widths from vacancy-scattering, plus Ag/Sb disorder scattering, are displayed in Fig. 8(b, c). It can be seen that $2\Gamma_{pd}$ is very small for small $\mathbf{q}$ and increases very fast for bigger $\mathbf{q}$, but it just contributes about 15% of the observed phonon line-width at 300 K. Therefore, vacancy scattering (plus Ag/Sb disorder) is not sufficient to account for the acoustic line-widths measured. It is possible that point-defect scattering has a stronger contribution to the scattering of optical modes, however, since it is expected to scale like $g(\omega)\,\omega^2$ (Refs. 47,48). Also, we emphasize that our model only considered single-defects. It is possible that more complex defects, including clusters of vacancies and anti-site defects, could have a larger contribution to the observed phonon scattering rates.

E. Minimum thermal conductivity

We note that the sound velocities, which were already reported in Ref. 32, are much smaller than the estimate of $4800\,ms^{-1}$ reported by Wolfe *et* al.[40] Averaging the sound velocity $\bar{c}_\eta$ over $\hat{\eta} = [001], [110], [111]$, according to ${}^3/\bar{c}_\eta^3 = {}^2/c_{\mathrm{TA}}^3 + {}^1/c_{\mathrm{LA}}^3$, we obtain $\bar{c}_{\mathrm{iso}} = 1640 \pm 30\,ms^{-1}$. As a result, the minimum thermal conductivity reported in Ref. 12 was considerably over-estimated. Using the q-dependent dispersions measured with INS, we estimated the minimum thermal conductivity within two approximations. In the first approximation, we set the mean-free-path Λ equal to the direction-dependent first-nearest-neighbor distance along [001], [110], and [111] respectively. This leads to $\kappa_{\min} = 0.16 \pm 0.02\,\mathrm{W}m^{-1}\mathrm{K}^{-1}$ at 300 K. A more realistic estimate corresponding to $\Lambda_j(\mathbf{q}) = v_j(\mathbf{q})\pi/\omega_j(\mathbf{q})$ (for τ equal to half an oscillation period) results in $\kappa_{\min} = 0.18 \pm 0.02\,\mathrm{W}m^{-1}\mathrm{K}^{-1}$. Thus,

the lattice thermal conductivity measured in $AgSbTe_2$ is three to four times larger than the minimum value. This is in agreement with the acoustic phonon excitations being still well defined, although broad, as discussed above.

IV. DIFFRACTION AND DIFFUSE SCATTERING

Further structural information concerning the ordering of cations, static or dynamic atomic displacements, and extended lattice defects were obtained from the neutron and synchrotron x-ray diffuse scattering measurements. We use reciprocal space coordinates (h, k, l) for an average underlying cubic rock-salt lattice throughout the discussion. In the elastic scattering channel of the single-crystal INS measurements (ARCS), $-1 < E < 1\,\mathrm{meV}$, we observe an obvious diffuse component between Bragg peaks, which extends across all the measured Brillouin zone (see Fig. 9 (a-c), logarithmic intensity scale). As can be seen in these panels, this diffuse component does not change with temperature. It is also very different from the thermal diffuse scattering contribution in the inelastic channel of the measurement, which is shown in Fig. 9 (d) for $T = 300\,\mathrm{K}$ and $1 < E < 20\,\mathrm{meV}$. The elastic component of the diffuse scattering corresponds to static deviations from the average ideal rock-salt structure, while the inelastic thermal diffuse scattering is due to phonons. The elastic component can be separated into several components, which were confirmed with synchrotron x-rays with a fine Q–resolution.

First, lobes of intensity with butterfly shapes are seen around the Bragg peaks of the average rock-salt lattice, indicative of strain. Second, sharp rods are seen in reciprocal $\langle 111 \rangle$ directions, and these were further characterized with synchrotron measurements, as discussed below. Third, we observe broad, weak reflections from superstructure (ordering of cations) at $\frac{1}{2}(h, k, l)$ with h, k, l odd, which are not expected for a rock-salt lattice. These correspond to L-points at the cubic Brillouin zone boundary along $\langle 111 \rangle$ directions in reciprocal space. They are broad, corresponding to real-space correlations of just a few nanometers. Moreover, transmission electron microscopy (TEM) measurements also confirm the short-ranged nature of the ordered nanodomains[32,33]. The half-integer peaks appear for elastic neutron scattering (energy integration range $-1 < E < 1\,\mathrm{meV}$). Thus, they are static in nature, as there are no phonon modes with such low energy at the L point. The static nature of this intensity can also be confirmed by considering its temperature dependence.

In the temperature dependence of the scattering function, Eq.(1), the temperature effect on the scattering intensity is mainly determined by the Debye-Waller factor for the elastic scattering ,

$$e^{-2W} = e^{-Q^2\langle u^2(T)\rangle/3}, \qquad (10)$$

where Q is the magnitude of the scattering vector,

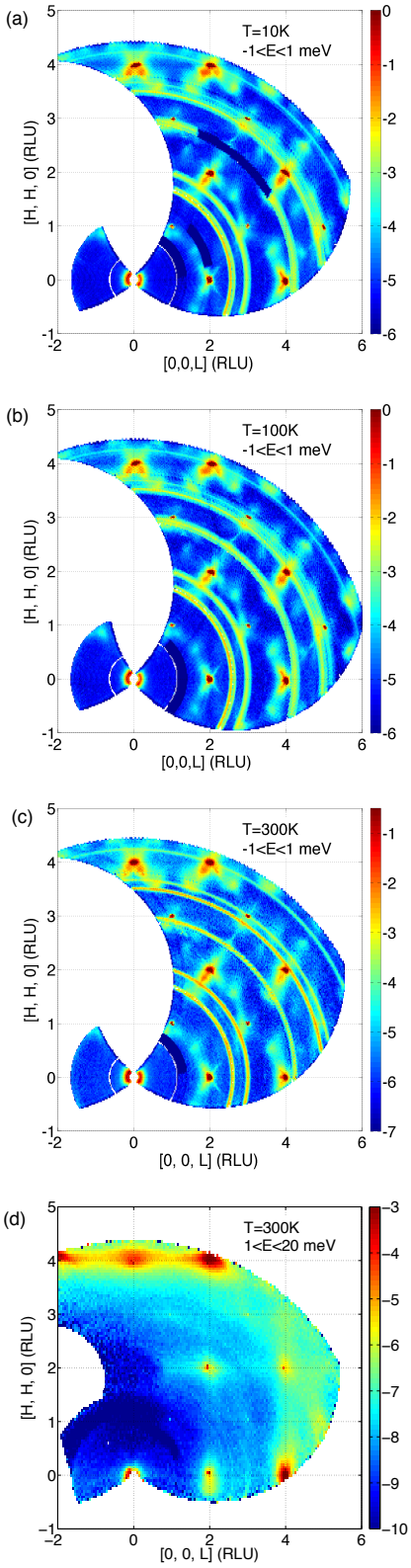

FIG. 9: (a,b,c) Neutron diffuse elastic scattering intensity for $Ag_{0.8}Sb_{1.2}Te_{2.2}$ at $T = 10, 100, 300\,\mathrm{K}$ ($-1 < E < 1\,\mathrm{meV}$). Dark arcs correspond to missing data. (d) Inelastic scattering at $T = 300\,\mathrm{K}$, integrated over $1 < E < 20\,\mathrm{meV}$). Reciprocal lattice units (RLU) are for an average rock-salt lattice.

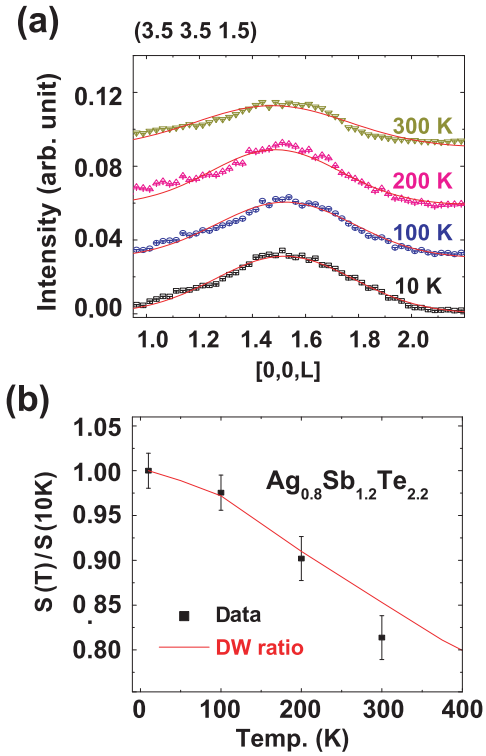

FIG. 10: (a) The temperature dependence of the $q = (\frac{7}{2}, \frac{7}{2}, \frac{3}{2})$ reflection in $Ag_{0.8}Sb_{1.2}Te_{2.2}$. (b) Relative change in intensity $S(T)/S_{10K}$ of the $(\frac{7}{2}, \frac{7}{2}, \frac{3}{2})$ peak versus T (black squares), compared with the effect from the Debye-Waller factor, based on the measured mean-square displacement $\langle u^2 \rangle_{iso}$ (from Ref. 32), showing good agreement.

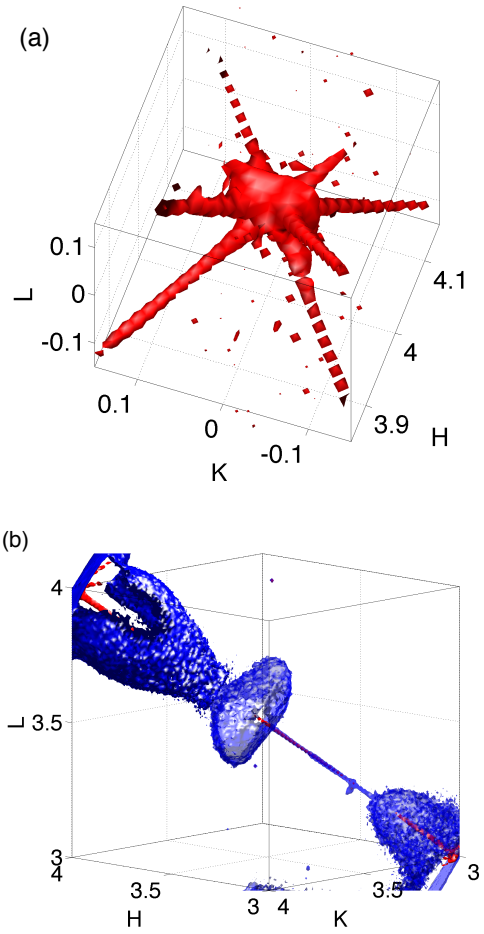

FIG. 11: X-ray diffuse scattering data (APS-33BM, 21.5 keV) measured on $Ag_{0.8}Sb_{1.2}Te_{2.2}$ at $T = 30$ K. (a) Three-dimensional view of diffuse scattering showing the sharp rods in reciprocal $\langle 111 \rangle$ directions around (400) Bragg peak. The discontinuities of rods are an artifact from the discretized rotations during data acquisition. (b) Three-dimensional view of diffuse scattering showing half-order reflection near $(\frac{7}{2}, \frac{7}{2}, \frac{7}{2})$, sharp rod along [111] (in red), and lobes around rock-salt peaks (444) and (333).

and $\langle u^2(T) \rangle$ is the temperature dependent mean-square-displacement. The intensity of the superlattice reflection at $(\frac{7}{2}, \frac{7}{2}, \frac{3}{2})$ is plotted as a function of temperature in Fig. 10(a,b). The suppression of the scattering intensity with increasing T can be calculated from the Debye-Waller factor by using the intensity at 10 K and the experimental T-dependent mean-square-displacement for $Ag_{0.8}Sb_{1.2}Te_{2.2}$ in Ref. 32. The result is given by the red curve in Fig. 10(b). The calculated scattering intensities of the L-point superlattices are in good agreement with the Debye-Waller effect (within experimental uncertainty), i.e. decreasing with temperature as the mean-square-displacements increase. This confirms that the origin of these half-order reflections is static (rather than thermal diffuse scattering, which would increase with T). We also did not observe any soft-mode at the L point in the phonon dispersions, ruling out the possibility of phonons of very low energy < 1 meV.

High-resolution views of the diffuse scattering were obtained with synchrotron x-ray diffuse scattering measurements (APS-33BM). X-ray diffuse scattering measurements do not discriminate between static (structure) and dynamic (phonons) components of the scattering intensity, but this information is provided by the four-dimensional $S(\mathbf{Q}, E)$ data from ARCS, as discussed above. Also, because the x-ray diffuse measurements were performed at low T (~ 30 K), the contribution from thermal diffuse scattering is minimized. Figures 11 (a,b) show three-dimensional renderings of the diffuse scattering intensity, revealing three different components. One can see sharp and intense rods along the cube body diagonals (in red), extended lobes around rock-salt Bragg peaks, and broad superstructure peaks half-way between Bragg peaks along the body diagonal (both in blue). In Fig. 11 (a), corresponding to a volume around the (400) Bragg peak, one can clearly see sharp, intense rods extending in $\langle 111 \rangle$ reciprocal directions. The same was seen

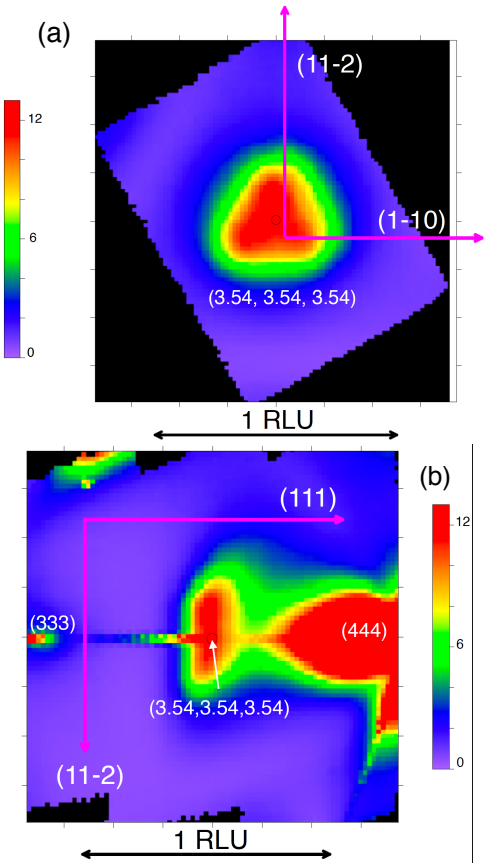

FIG. 12: X-ray diffuse scattering data (APS-33BM, 21.5 keV) measured on $Ag_{0.8}Sb_{1.2}Te_{2.2}$ at $T = 30$ K, showing two-dimensional cuts through half-order reflection near $(\frac{7}{2}, \frac{7}{2}, \frac{7}{2})$, parallel to (111) in (a) and (1-10) in (b) reciprocal planes.

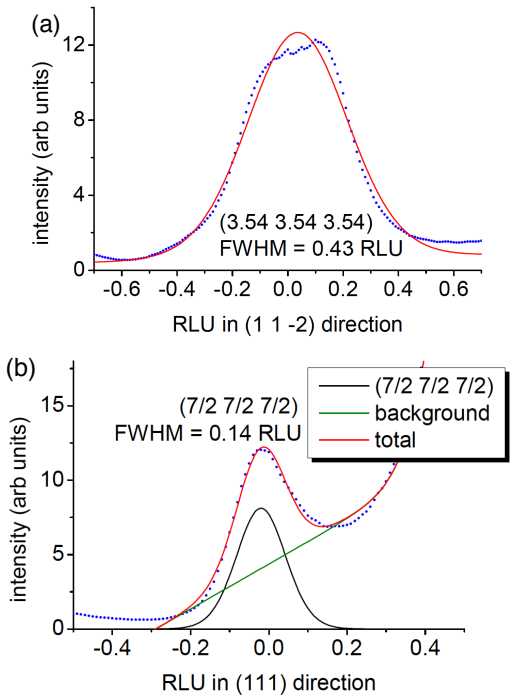

FIG. 13: X-ray diffuse scattering data (APS-33BM, 21.5 keV) measured on $Ag_{0.8}Sb_{1.2}Te_{2.2}$ at $T = 30$ K. (c) and (d): one-dimensional cuts vertically through the $(\frac{7}{2}, \frac{7}{2}, \frac{7}{2})$ reflection of (a), and horizontally through the slice in (b), respectively.

around other $(H, 0, 0)$ Bragg peaks. For other types of Bragg peaks, such as (2,2,0) or (2,2,2), only a subset of the rods could be seen, corresponding to strong intensity for rods that are most collinear with **Q**. This is what is expected from extended planar defects (faults) in {111} planes, with atomic displacements normal to the planes. The faults must be laterally extended to large distances, and have well-defined, narrow thickness in order to give rise to such sharp, extended rods. Previous studies of $Ag_{1-x}Sb_{1+x}Te_{2+x}$ for $x \sim 0.2$ reported Te-Te double layers in (111) planes[21,22], and it is possible that such extended defects give rise to the rods. Because of their narrow width, the rods have to be much more extended laterally than the nano-domains seen in TEM, which is compatible with the Te sublattice being coherent across the Ag/Sb ordering nanodomains. Our current analysis of the intensity of the rods suggests that the density of the planar defects is low, however, which suggests that they should not be a dominant source of phonon scattering. The strains, which are most pronounced in ⟨111⟩ directions, may be more important in suppressing the phonon mean-free-paths in these directions.

The half-order reflections at L points were clearly observed in the synchrotron data. For example, the superstructure peak around $(\frac{7}{2}, \frac{7}{2}, \frac{7}{2})$ is shown in Figs. 11(b), and 12(a,b). Similar superlattice peaks were observed at all L points in the synchrotron experiment (about 10 locations measured), in agreement with the neutron data of Fig. 10 (a-c). The occurrence of reflections at these half-order positions is compatible with several proposed superstructures for ordering of the cations. In particular, our observations are compatible with the $L1_1$ and D4 superstructures proposed by Barabash *et* al. and Hoang *et* al.[25,26,28]. The simpler $L1_1$ superstructure corresponds to a segregation of Ag and Sb cations into alternating {111} planes. We also observe a small but significant displacements of the broad superstructure peaks from precise half-order positions, the origin of which is currently unknown. In addition, the observed relative intensities show deviations from the expected values for the $L1_1$ and D4 superstructures. The difference between the rock-salt, $L1_1$, and D4 structures is primarily in the arrangement of the three elements on a simple-cubic lattice. As we will discuss in a subsequent publication, the deviations in half-order intensities could indicate a disruption of the underlying simple-cubic lattice.

The high-Q resolution and signal/noise ratio provided by synchrotron radiation allow accurate determination of peak width. As shown in Fig. 12(a,b), the half-order

peaks from cation ordering are broad and disk-shaped. Each half-order reflection lies on a line in a $\langle 111 \rangle$ reciprocal space direction, joining all-even $(2l, 2n, 2m)$ and all-odd $(2l \pm 1, 2m \pm 1, 2n \pm 1)$ Bragg reflections of the underlying average rocksalt lattice. Cuts through the superlattice half-order peaks along $[1, 1, \bar{2}]$ and $[1, 1, 1]$ reciprocal directions are shown in Figs. 13(a,b). The diffuse reflections are sharper in the (111) direction: 0.14 reciprocal lattice unit (RLU) full-width-at-half-maximum (FWHM). They are broader in the transverse (1 -1 0) reciprocal-space directions: 0.43 RLU FWHM. In real-space, this corresponds to longer correlations for the ordering along $\langle 111 \rangle$ chains, but still limited to a few nanometers. Close examination of 12(a,b) shows that the half-order reflections have a triangular profile and small but significant displacements from precise half-order positions. Thus, the broad profiles may be a combination of sharper reflections from different domains. The local ordering of Ag and Sb leads to a relaxation of the atomic positions away from the underlying rock-salt lattice[32]. The resulting large, temperature-independent atomic-displacements were also revealed with Rietveld refinements of neutron powder diffraction data[32]. Because the ordered domains are only a few nanometers across, these atomic relaxations are disorganized, and could lead to lattice strains that give rise to the extended lobes around primary Bragg peaks, clearly seen in both neutron (Fig. 9 (a-c)) and x-ray (Fig. 11 (b)) single-crystal measurements.

We point out that the cation short-range ordering has a correlation length comparable or shorter (a few unit cells) than the mean-free-paths of acoustic phonons which dominate thermal transport ($\gtrsim 50\,\text{Å}$)[32]. The ordering correlation length is even shorter than the wavelength for some of these acoustic phonons. As a result, the heat-carrying phonons should be seen as excitations of the average structure, rather than a superposition of spatially-distinct excitations in separate low-symmetry twin variants. On the other hand, if the size of ordered domains were much larger than the wavelength and mean-free-path, we would expect the phonon linewidths to become sharper, and the dispersions to develop the symmetry of the ordered phase.

V. CONCLUSION

The structure and phonon spectra of the thermoelectric material $Ag_{1-x}Sb_{1+x}Te_{2+x}$ (x = 0, 0.1, 0.2) were investigated with a comprehensive suite of neutron and x-ray scattering measurements. From our analysis of the phonon DOS, dispersions, and phonon lifetimes, the contributions of anharmonic phonon-phonon and point-defect (single vacancy plus Ag/Sb disorder) scattering processes were assessed. We conclude that anharmonicity is not the dominant contribution to the phonon scattering rates from 10 to 300 K. The observation of broad half-order superlattice peaks and diffuse scattering confirms reports from electron-microscopy[32,33]. These results support the view that a complex nanostructure, resulting from ordering of cations limited to short-ranged correlations, and which introduces correlated atomic displacements, interfaces, and strains, constitutes the dominant source of phonon scattering at room temperature and below.

ACKNOWLEDGEMENTS

Work at ORNL was supported by the US DOE, Office of Basic Energy Sciences, Materials Sciences and Engineering Division (O.D., E.D.S, A.F.M., J.D.B., M.A.M.) and also through the S3TEC Energy Frontier Research Center, DESC0001299 (J.M.). O.G. thanks the Lujan Neutron Scattering Center at LANSCE, which was funded by the US DOE Office of Basic Energy Sciences (DOE). Los Alamos National Laboratory is operated by Los Alamos National Security LLC under DOE Contract DE-AC52-06NA25396. The use of Oak Ridge National Laboratory's SNS and HFIR was sponsored by the Scientific User Facilities Division, Office of Basic Energy Sciences, US Department of Energy. Use of the APS, an Office of Science User Facility operated for the U.S. DOE Office of Science by ANL, was supported by the U.S. DOE under Contract No. DE-AC02-06CH11357.

Appendix A: Experimental Details

1. Synthesis

All samples were prepared from the stoichiometric mixture of 99.999% tellurium and antimony, and 99.8% silver. Powder samples were prepared by direct fusion in sealed, evacuated, carbon-coated silica tubes. They were melted at 1,000°C for 24h, gradually cooled down to 550°C, and rapidly cooled down by quenching in water. Single crystals were synthesized by a modified Bridgmann technique in silica ampoules with a tapered end. The elements were heated to 1000°C for 12 h, cooled to 645°C at 25°C/h, held for two hours at 645°C, then cooled to 545°C at 0.4°C/h. After being held at 545°C for 12 h, the crystals were removed from the furnace and cooled in air inside their ampoules. Large single crystals ($\sim 15\,g$) were obtained for $x = 0.1$ and 0.2, while stoichiometric crystals of $AgSbTe_2$ were generally smaller, $\sim 1\,g$.

2. Characterization

The transport properties were measured on bars cut from single-crystals, using a Quantum Design Physical Property Measurement System (PPMS), as discussed in Ref. 32. We find $0.55 \leqslant \kappa_{\text{tot}} \leqslant 0.75\,\text{W}m^{-1}\text{K}^{-1}$, increasing monotonically with T in the range $50 \leqslant T \leqslant 200\,\text{K}$, in good agreement with prior reports[11,12,14]. The increase

in $\kappa_{\rm tot}$ with T can be accounted for by the electron, hole, and ambipolar terms in $\kappa_{\rm el}$, as reported by Jovovic *et al.*[10] As a result, $\kappa_{\rm lat}$ is weakly dependent on T, with $\kappa_{\rm lat} \simeq 0.65\,{\rm W}m^{-1}{\rm K}^{-1}$ around 200 K.

Both NPD patterns and EPMA composition maps indicate that the samples with nominal compositions of $AgSbTe_2$ and $Ag_{0.9}Sb_{1.1}Te_{2.1}$ are comprised of a main phase corresponding to the δ phase in the (Ag, Sb, and Te) ternary phase diagram[19] and a small amount of monoclinic Ag_2Te (about 6% Ag_2Te in $AgSbTe_2$ and 2% Ag_2Te in $Ag_{0.9}Sb_{1.1}Te_{2.1}$) as reported in Ref. 13, while only the δ–phase is observed in $Ag_{0.8}Sb_{1.2}Te_{2.2}$. The absence of Ag_2Te in $Ag_{0.8}Sb_{1.2}Te_{2.2}$ was also confirmed with differential scanning calorimetry. In addition, composition maps from electron-microprobe analysis show that most of the Ag_2Te secondary phase segregates into lamellae at the end of the ingot from eutectic decomposition[24,32].

* delaireoa@ornl.gov

1 H. J. Goldsmid, *Introduction to Thermoelectricity* (Springer, Berlin, 2010).
2 G. J. Snyder and E. S. Toberer, Nature Materials **7**, 105 (2008).
3 C. Wood, Rep. Prog. Phys. **51**, 459 (1988).
4 B. C. Sales, O. Delaire, M. A. McGuire, and A. F. May, Phys. Rev. B **83**, 125209 (2011).
5 O. Delaire, K. Marty , M. B. Stone, P. R. C. Kent, M. S. Lucas, D. L. Abernathy, D. Mandrus, B. C. Sales, Proc. Natl. Acad. Sci. USA **108**, 4725 (2011).
6 Yanzhong Pei, Xiaoya Shi, Aaron LaLonde, Heng Wang, Lidong Chen, and G. Jeffrey Snyder, Nature **473**, 66–69 (2011).
7 T. Shiga, J. Shiomi, J. Ma, O. Delaire, T. Radzynski, A. Lusakowski, K. Esfarjani, and G. Chen, Phys. Rev. B **85**, 155203 (2012).
8 T. Shiga, T. Murakami, T., O. Delaire, and J. Shiomi, Appl. Phys. Express **7**, 041801 (2014).
9 C.W. Li, O. Hellman, J. Ma, A.F. May, H. B. Cao, X. Chen, A.D. Christianson, G. Ehlers, D.J. Singh, B.C. Sales, and O. Delaire, Phys. Rev. Letters **112**, 175501 (2014).
10 V. Jovovic and J. P. Heremans, Phys. Rev. B 77, 245204 (2008).
11 E. F. Hockings, Phys. Chem. Solids 10, 341 (1959).
12 D. T. Morelli, V. Jovovic, and J. P. Heremans, Phys. Rev. Lett. 101, 035901 (2008).
13 S. Zhang, T. Zhu, S. Yang, C Yu and X. Zhao, Acta Mater. **58**, 4160-4169 (2010).
14 S.N. Zhang, T.J. Zhu, S.H. Yang, C. Yu, X.B. Zhao, J. Alloys and Compounds **499**, 215-220 (2010).
15 V. Zhuse, V. Sergeeva, and E. Shtrum, Sov. Phys. Tech. Phys. **3**, 1925(1958) .
16 K. F. Hsu, S. Loo, F. Guo, W. Chen, J. S. Dyck, C. Uher, T. Hogan, E. K. Polychroniadis, M. G. Kanatzidis, Science, **303**, 818 (2004).
17 M. D. Nielsen, V. Ozolins, and J-P. Heremans, Energy Environ. Sci. **6**, 570 (2013).
18 Lin-Hui Ye, K. Hoang, A. J. Freeman, S. D. Mahanti, J. He, T. M. Tritt, and M. G. Kanatzidis, Phys. Rev. B **77**, 245203 (2008).
19 J. Sugar and D. Medlin, J. of All. and Comp. **478**, 75 (2009).
20 D. Medlin and J. Sugar, Scrip. Mater. **62**, 379 (2010).
21 P.A. Sharma, J, Sugar, D. Medlin, J. Appl. Phys. **107**, 113716 (2010).
22 J. Sugar and D. Medlin, J. Mater. Sci. **46** 16681679 (2011).
23 R. G. Maier, Zeitschrift für Metallkunde **54**, 311 (1963).
24 R-M. Marin, G. Brun, and J-C. Tedenac, J. Mater. Sci. **20**, 730 (1985).
25 S. V. Barabash, V. Ozolins, and C. Wolverton, Phys. Rev. Lett. **101**, 155704 (2008).
26 S. V. Barabash and V. Ozolins, Phys. Rev. B **81**, 075212 (2010).
27 E. Quarez, K.-F. Hsu, R. Pcionek, N. Frangis, E. K. Polychroniadis, and M. G. Kanatzidis, J. Am. Chem. Soc. **127**, 9177 (2005).
28 K. Hoang, S. D. Mahanti, J. R. Salvador, and M. G. Kanatzidis, Phys. Rev. Lett. **99**, 156403 (2007).
29 O. Delaire, J. Ma, K. Marty, A. F. May, M. A. McGuire, M-H. Du, D. J. Singh, A. Podlesnyak, G. Ehlers, M. D. Lumsden, and B. C. Sales, Nature Materials **10**, 614 (2011).
30 C.W. Li, O. Hellman, J. Ma, A.F. May, H. Cao, X. Chen, A.D. Christianson, G. Ehlers, D.J. Singh, B.C. Sales, and O. Delaire, Phys. Rev. Letters **112**, 175501 (2014).
31 J.W.L. Pang, W.J.L. Buyers, A. Chernatynskiy, M.D. Lumsden, B.C. Larson, and S.R. Phillpot, Phys. Rev. Lett. **110**, 157401 (2013).
32 J. Ma, O. Delaire, A. F. May, C. E. Carlton, M. A. McGuire, L. H. VanBebber, D. L. Abernathy, G. Ehlers, Tao Hong, A. Huq, Wei Tian, V. M. Keppens, Y. Shao-Horn, and B. C. Sales, Nature Nanotechnology **8**, 445 (2013).
33 C. E. Carlton, R. De Armas, J. Ma, A. F May, O. Delaire and Yang Shao-Horn, J. Appl. Phys. **115**, 144903 (2014)
34 A. Huq, J. P. Hodges, O. Gourdon, L. Heroux, Z. Kristallogr. Proc. **1**, 127 (2011).
35 A. C. Larson, R.B. von Dreele, General Structure Analysis System (GSAS), Los Alamos National Laboratory, Los Alamos, NM, USA, 1990. B. H. Toby, J. Appl. Crystallogr. 34, 210-213 (2001).
36 D. L. Abernathy, M. B. Stone, M. J. Loguillo, M. S. Lucas, O. Delaire, X. Tang, J.Y.Y. Lin, and B. Fultz, Rev. Sci. Instrum. **83**, 15114 (2012).
37 Ehlers G., Podlesnyak A. A., Niedziela J. L., Iverson E. B., Sokol P. E., Review of Scientific Instruments **82**, 85108 (2011).
38 G. L. Squires, *Introduction to the Theory of Thermal Neutron Scattering* (Cambridge University Press, Cambridge, 1978).
39 O. Delaire and C. Stassis, "Phonon Studies" in "Characterization of Materials" (Wiley, 2012).
40 R. Wolfe, J. H. Wernick, and S. E. Haszko, J. Appl. Phys. **31**, 1959 (1960).
41 E. Karapetrova, G. Ice, J. Tischler, H. Hong, P. Zschack, Nucl. Instrum. Methods Phys. Res. A **649**, 52-54 (2011).
42 G. Grimvall, *Thermophysical Properties of Materials* (North Holland, 1999).
43 T. M. Tritt, "Thermal Conductivity: theory, properties,

and applications" (Kluwer Academic/Plenum Publishers, 2004).
[44] R. Peierls, Ann. Phys., Leipzig 3, 1055 (1929).
[45] G. Leibfried and E. Schlomann, Nachr. Akad. Wiss. Gottingen II **a(4)**, 71 (1954).
[46] G. Slack, and S. Galginaitis, Phys. Rev. **133**, 253 (1964).
[47] P. G. Klemens, "Thermal Conductivity and Lattice Vibrational Modes", in "Solid State Physics, Advances in Research and Applications", Eds. F. Seitz and D. Turnbull, vol. 7, pp. 1–98 (1958).
[48] S. Tamura, Phys. Rev. B **27**, 858 (1983).